Condensation of indirect excitons

L.V. Butov

L.V. Butov, University of California, San Diego, USA; lvbutov@physics.ucsd.edu

An indirect exciton (IX), also known as an interlayer exciton, is a bound pair of an electron and a hole confined in spatially separated layers. Due to their long lifetimes, IXs can cool below the temperature of quantum degeneracy. This provides an opportunity to experimentally study cold composite bosons. This article overviews our studies of cold IXs, presenting spontaneous coherence and Bose–Einstein condensation of IXs and phenomena observed in the IX condensate, including the spatially ordered exciton state, commensurability effect of exciton density wave, spin textures, Pancharatnam–Berry phase, long-range coherent spin transport, and interference dislocations.

Keywords: heterostructure, optical properties, 2D materials

Introduction

An exciton is a bound pair of an electron and a hole. At low densities, $n << 1/a_B^D$ (a_B is the exciton Bohr radius and D the dimensionality), excitons are hydrogenlike Bose particles. Since the temperature of quantum degeneracy scales inversely with the mass, and the exciton mass is small, the quantum degeneracy in excitons can be achieved at temperatures ~ 1 K in conventional semiconductors, orders of magnitude larger than the microkelvin temperatures for atoms. 2,3

In order to create cold excitons, we work with IXs in coupled quantum well (CQW) heterostructures (**Figure 1**a). The separation between the electron and hole layers leads to long IX lifetimes. Within their long lifetimes, IXs can cool below the temperature of quantum degeneracy.⁴ In experiments with IXs in GaAs CQW overviewed in this article, IXs can cool to ~0.1 K, below the

1

temperature of quantum degeneracy T_q ($T_q = 2\pi\hbar^2 n/m \approx 3$ K for the exciton mass $m = 0.22m_0$, m_0 is the mass of a free electron, and density per spin state $n = 10^{10}$ cm⁻² relevant to the experiments; \hbar is the reduced Planck constant).⁵ IXs are dipoles oriented perpendicular to the QW plane; the dipolar repulsive interaction between IXs stabilizes the exciton state against the formation of metallic electron—hole droplets.⁶ These properties make IXs a suitable system for studying cold bosons in condensed-matter materials.

Spontaneous coherence and Bose-Einstein condensation of indirect excitons

If bosonic particles are cooled below the temperature of quantum degeneracy, they can spontaneously form a coherent state in which their matter waves synchronize and combine. Spontaneous coherence of matter waves is equivalent to condensation of particles in momentum space referred to as Bose–Einstein condensation (BEC). Coherence between excitons separated in the CQW plane by δx is quantified by the first order coherence function $g_1(\delta x)$. The Fourier transform of the $g_1(\delta x)$ gives the particle distribution in momentum space n_k . The width of $g_1(\delta x)$, the coherence length ξ , is inversely proportional to the width of n_k . In a classical gas, ξ is close to the thermal de Broglie wavelength $\lambda_{\rm dB} = (2\pi\hbar^2/mT)^{1/2}$ and is small ($\xi_{\rm classical} = \lambda_{\rm dB}/\pi^{1/2} \sim 0.3$ µm at T = 0.1 K for IXs in GaAs CQW). The measurement of spontaneous coherence with $\xi >> \xi_{\rm classical}$ is a direct measurement of BEC. In earlier studies, evidence for spontaneous coherence was obtained for IXs in CQWs⁷ and for IXs in quantum Hall bilayers. ^{8,9} The onset of spontaneous coherence was evidenced by a strong enhancement of the rates of IX radiative recombination⁷ and electron tunneling, ⁸ respectively.

Direct measurements of spontaneous coherence are performed in interferometric experiments. Excitons transform to photons, which inherit their coherence, therefore, exciton coherence can be measured by probing coherence of their light emission. An enhancement of the IX coherence length at low temperatures was first measured in interferometric experiments in a study reported in Reference 10. These experiments used the single-pinhole

interferometric technique, which does not measure $g_1(\delta x)$, and the derivation of ξ was based on a mathematical analysis of the data.^{10,11}

The direct measurement of spontaneous coherence (i.e. BEC, in a gas of IXs) was performed in another study (Reference 12). In this work, the pattern of $g_1(\delta x)$ is measured by shift interferometry. The emission images produced by each of the two arms of the Mach–Zehnder interferometer are shifted with respect to each other to measure the interference between the emission of IXs spatially separated by δx in the CQW plane.

The measured amplitude of interference fringes $A_{\text{interf}}(\delta x)$ is given by the convolution of $g_1(\delta x)$ with the point-spread function (PSF) of the optical system. The PSF width corresponds to the spatial resolution (~1.5 µm in this experiment). The measurements of $A_{\text{interf}}(\delta x)$ in IX condensate and classical IX gas are presented in Figure 1b by black squares and blue circles, respectively. For a classical IX gas, $g_1(\delta x)$ is narrow and $A_{\text{interf}}(\delta x)$ fits well to the PSF, which is shown by the blue line. For the IX condensate, $g_1(\delta x)$ and, in turn, $A_{\text{interf}}(\delta x)$ extend to large δx , demonstrating spontaneous coherence. The interference of the

Figure 1c presents $g_1(\delta x)$ for a classical gas (blue dashed line) and for a quantum gas (black dashed line); both curves are computed for a spatially homogeneous gas of noninteracting particles with a quadratic dispersion. Both gases are at 0.1 K; the occupation number of the k = 0 state (n_0) is <<1 for the classical gas and 5,000 for the quantum gas. The convolution of these $g_1(\delta x)$ with the PSF produces data shown as black and blue solid lines, which fit to measured $A_{\text{interf}}(\delta x)$ in the quantum IX gas and in the classical IX gas, respectively (Figure 1b–c). The Fourier transform of $g_1(\delta x)$ in Figure 1c gives n_k shown in Figure 1d. n_k in the condensate is much narrower than in the classical gas (Figure 1d).

Shift-interferometry is a powerful method to measure spontaneous coherence (i.e., BEC, of excitons). Measuring the spatial map of $g_1(\delta x)$ and, in turn, its width ξ , gives a map of the condensate. The regions of a classical gas in the $\xi(x,y)$ pattern correspond to the smallest observed coherence length. The condensate regions have coherence length much larger than in a classical gas. In Ref. 12, the coherence length in the condensate regions reaches ca. 10 μ m, $\xi_{classical}$

 $\sim 0.3~\mu m,$ the smallest observed coherence length is given by the PSF width $\sim 1.5~\mu m.$

We studied IX condensation in two systems where a cold IX gas is realized: in exciton rings ^{10,12} and in a diamond-shaped electrostatic trap. ¹³ The exciton rings are described later in Section *Spatially ordered exciton state*. Mapping the IX condensate in these experiments shows that a classical IX gas is observed at high temperatures, above the condensation temperature, or in the hot areas where IX gas is heated due to the IX generation, while the IX condensate is observed at low temperatures, below the condensation temperature, in the regions separated from the hot areas of IX generation. ¹² For IXs in the trap, the IX condensate is observed at low temperatures in the trap center separated from the hot exciton generation area. ¹³ The measured IX condensation temperature reaches a few K. ^{10,12,13}

IX condensation in a trap has been considered theoretically. ¹⁴ The model ¹⁴ considers (quasi)equilibrium distribution of IXs over states in the trap taking into account the effect of screening of the trap potential by IXs. The theoretical studies ¹⁴ were applied to a system of IXs in the trap where exciton condensation was studied in experiments. ¹³ The theoretical estimate for the condensation temperature ¹⁴ is in qualitative agreement with the experimental results: the estimated condensation temperature $\sim 0.3-1~{\rm K}^{13}$; in the experiment, with lowering the temperature, the exciton coherence length starts to increase relative to the high-temperature classical value around 2 K and at T $\sim 1~{\rm K}$ the extension of coherence over the entire IX cloud is observed ¹³. The qualitative agreement between the theoretical estimates ¹⁴ and experimental measurements ¹³ of IX condensation indicates that IX condensation can be adequately described by the theory based on (quasi)equilibrium Bose–Einstein distribution of interacting bosons.

Phenomena observed in the condensate of indirect excitons

The phenomena emerging in the IX condensate include the spatially ordered exciton state, ¹⁵ commensurability effect of exciton density wave, ¹⁶ spin textures, ¹⁷

Pancharatnam—Berry phase and long-range coherent spin transport, ¹⁸ and interference dislocations. ¹⁹ These phenomena are presented below.

Spatially ordered exciton state

A spatially ordered excitonic state was observed in which the exciton density undergoes modulational instability.¹⁵ This state, dubbed the macroscopically ordered exciton state (MOES), exhibits approximately periodic spatial modulation over lengths up to 1 mm within an exciton ring (**Figure 2**). The MOES forms when the IX gas is cooled below a few Kelvin.

The experiments revealed the following MOES properties. (1) The exciton coherence length in the MOES reaches micrometers, ^{10–12,20} an order of magnitude greater than the coherence length that can be achieved in a classical exciton gas. showing that the MOES is a condensate in momentum-space (Section Spontaneous coherence and Bose–Einstein condensation of indirect excitons). (2) The MOES forms in the external ring of the exciton pattern formation. ¹⁵ The external ring itself forms on the interface between the electron-rich and hole-rich regions^{21,22} (the hole-rich region is inside the external ring and the electron-rich region is outside the external ring in^{21,22}). This interface is essential for the MOES since no spontaneous density modulation is observed in another exciton ring—the inner ring, where no such interface is involved. 15,23 (3) The MOES is characterized by repulsive IX interaction.²⁴ This is consistent with the predicted repulsive interaction between IXs. Repulsive interaction forms a negative feedback to density fluctuation, thus acting against density modulation (repulsive interaction forces particles to move from the regions of higher densities to the regions of lower densities, thus forming a negative feedback to density fluctuation and making the density spatially homogeneous).

A search for a mechanism responsible for the formation of the MOES led to a model attributing a modulational instability to stimulated processes of exciton formation at the interface between the electron-rich and hole-rich regions that build up near quantum degeneracy.²⁵ This model is in agreement with all experimental data. It is in agreement with data (1–3i), listed in the previous paragraph and it predicts the modulation wavelength to be of the order of the

external ring width, which compares favorably with the measured luminescence profile at the external ring.²¹

The MOES disappears above the IX condensation temperature where the ring becomes trivial with no periodic spatial modulation. ^{12,15} This is consistent with the requirement for the density modulation of the stimulated processes, which rate is enhanced with the exciton state occupation, that is provided by the condensate with high exciton state occupation. ²⁵

Commensurability effect of exciton density wave

The exciton density in the ring is controlled by the laser excitation power and applied voltage.²¹ Increasing the exciton density leads to an increase of the MOES wavelength λ_c ,¹⁶ in agreement with the model in Ref. 25.

Besides the external ring and inner ring, the exciton pattern formation also includes localized bright spots (LBSs), which are associated with electron current filaments across the sample (the electrons provided by these current filaments to the hole-rich region bind to the holes creating IXs).²¹ LBS beads (i.e. beads of IX luminescence at LBSs) are stable while MOES beads fluctuate with time, ¹⁶ showing that the phase of the exciton density wave is locked at LBSs and fluctuates in between them. Confining the MOES segment on length L between two LBSs and controlling λ_c allows varying L/λ_c and, as a result, probing how commensurability between L and λ_c affects the exciton density wave.

The commensurability effect was observed. The fluctuations of exciton density wave are suppressed when the number of wavelengths of the exciton density wave confined between two LBSs, $v = L/\lambda_c$, is an integer. The stability of the confined exciton density wave was also analyzed by numerical simulations and the commensurability effect was found within the model describing the exciton density wave in terms of an instability due to stimulated processes.

The MOES is a state with spontaneously broken symmetry involving a large number of excitons ($\sim 10^6$ in the ring segment considered in Reference 16). The coherence length in the MOES is an order of magnitude greater than in a classical exciton gas, identifying MOES as a condensate. However, the

coherence length ξ in the MOES is limited to micrometers and is smaller than the MOES wavelength λ_c reaching tens of micrometers. ¹⁶ The commensurability effect presents collective behavior of the entire macroscopic system of excitons in the external ring segment of length ~100 μ m containing several MOES wavelengths. ¹⁶ The commensurability effect shows that the MOES is a collective phenomenon.

Spin textures

Long-range spin textures (spin patterns) were observed in a coherent gas of IXs around the exciton rings. ¹⁷ The spin textures result in the appearance of a variety of polarization patterns, including helical patterns, four-leaf patterns, spiral patterns, bell-like patterns, and periodic patterns. ¹⁷ The helical polarization patterns are shown in Figure 3c-d; the other patterns are discussed in Reference 17. As outlined in Section Pancharatnam-Berry phase and long-range coherent *spin transport*, the long-range spin textures and associated polarization patterns emerge due to the suppression of spin relaxation in the IX condensate. All observed spin textures and polarization patterns are described by a theoretical model based on ballistic IX transport and coherent precession of spins of electrons and holes. ¹⁷ The former originates from the suppression of scattering in IX condensate¹² (Section Spontaneous coherence and Bose–Einstein condensation of indirect excitons) and the latter from the suppression of spin relaxation in IX condensate¹⁷ (Section Pancharatnam–Berry phase and long-range coherent spin transport). The spin textures and polarization patterns disappear above the IX condensation temperature. 17 This is consistent with the requirement of long-range ballistic IX transport and long-range coherent spin precession that is provided by the condensate. 17

Pancharatnam-Berry phase and long-range coherent spin transport

The Pancharatnam–Berry phase^{26,27} is a geometric phase. The Pancharatnam–Berry phase appears when the polarization state of light changes.²⁶ This connection of the Pancharatnam–Berry phase to polarization makes it an intrinsic phenomenon for polarization textures.

To uncover the Pancharatnam-Berry phase in a condensate of IXs, we have explored LBSs¹⁸. As discussed in "Spatially ordered exciton state" and "Commensurability effect of exciton density wave" subsections, a cold gas of IXs is realized in regions of the external ring and LBS rings¹². LBS sources are stable sources of cold IXs¹⁶ and thus are a suitable system for exploring phenomena in exciton condensates.

While a more detailed picture is obtained by measuring $g_1(\delta x)$, as described in Section Spontaneous coherence and Bose–Einstein condensation of indirect excitons, mapping IX condensate can be done by measuring $A_{\text{interf}}(x,y)$ at one value of δx chosen to exceed both λ_{dB} and the PSF width. For such δx , a low A_{interf} is observed for a classical gas and a high A_{interf} for the condensate. For the parameters of our system, $\delta x = 2 \mu \text{m}$ is optimal for this experiment.

The IX gas is—classical close to the heating sources in the LBS central region (this heating is due to the current filament at the LBS center and the binding energy released at IX formation²¹). This is revealed by the small amplitude of interference fringes A_{interf} at $r < r_{\text{coh}}$ (**Figure 3**e,f). Away from the heating sources, IXs cool down and approach the condensation temperature at $r = r_{\text{coh}}$, where A_{interf} sharply rises, indicating condensation.

The exciton source at LBSs can be controlled by excitation power and voltage. ¹⁶ This allows varying r_{coh} , which increases with enhanced heating at the LBS central region for the enhanced source. ¹²

A ring of linear polarization is seen for each LBS in the region $r < r_{\text{linear}}$. (Figure 3c,d) The IX gas is classical in this region since $r_{\text{linear}} = r_{\text{coh}}$ (Figure 3c-f). This linear polarization originates from the distribution of IXs over the linearly polarized IX states.¹⁷ A helical IX polarization texture winding by 2π around the origin (i.e., a vortex of linear polarization), emerges at $r > r_{\text{linear}}$, showing that the polarization textures appear in the IX condensate¹⁷ (Figure 3c-f).

Figure 3a-b shows that the phase of interference fringes sharply changes at distance from the LBS center $r = r_{\text{phase}}$. For a broad range of r_{phase} and r_{linear} variations, $r_{\text{phase}} = r_{\text{linear}}$, indicating that the phase shifts of the interference fringes are observed when the polarization state of IX emission sharply changes. ¹⁸

The interference patterns allow a map of IX momentum describing the evolving IX phase in the vicinity of a source to be obtained. This map shows that IXs propagate away from the LBS source and sharply acquire an additional evolving phase $\phi = kr$ at $r = r_{\text{phase}}$.

The experiment shows that $r_{\rm phase} = r_{\rm linear} = r_{\rm coh}$, i.e. that the phase shifts correlate with the polarization pattern of IX emission and onset of IX spontaneous coherence¹⁸ (Figure 3 and more data in Reference ¹⁸). The correlation between the phase shift and the polarization change identifies the phase as the Pancharatnam–Berry phase acquired in a condensate of IXs.

The electron–hole spatial separation in IX suppresses the spin relaxation mechanism due to electron–hole exchange. 28 In a classical IX gas, spin transport in the studied structure is limited by $1-2 \mu m^{29}$ due to Dyakonov–Perel spin relaxation associated with scattering. As a result, for uncondensed IXs at $r < r_{\rm coh}$, the spin relaxation is fast and coherent spin precession is not observed. However, the suppression of scattering in IX condensate results in the suppression of the spin relaxation, enabling long-range coherent spin transport in IX condensate. Therefore, IX condensation at $r > r_{\rm coh}$ dramatically enhances the electron and hole spin relaxation time, leading to coherent spin precession and, in turn, precession of the polarization state of IX emission. This precession generates the evolving Pancharatnam–Berry phase of IXs, which is detected as the shift of interference fringes. No decay of the evolving Pancharatnam–Berry phase is observed over macroscopic lengths exceeding $10 \mu m$. This indicates the achievement of macroscopic long-range coherent spin transport in the IX condensate.

The observed spin textures and polarization patterns (Section *Spin textures*) and Pancharatnam–Berry phase (Section *Pancharatnam–Berry phase and long-range coherent spin transport*) in IX condensate are described by the theoretical model reported in Reference 17. Within this model, ballistic IX transport and coherent precession of spins of electrons and holes lead to the oscillatory behavior of polarization of IX emission. ^{17,18} Its long-scale component is responsible for the polarization patterns (Figure 3c–d). ¹⁷ The short-scale component has a spatial period that cannot be resolved with the optical resolution

in the imaging experiment.¹⁸ However, these fast changes of polarization generate the evolving Pancharatnam–Berry phase of IXs revealed in the interference experiment (Figure 3a–b).¹⁸

The sharp phase shifts associated with the Pancharatnam–Berry phase of IXs disappear above the IX condensation temperature where the interference patterns become trivial with no such shifts. This is consistent with the requirement of long-range ballistic IX transport and long-range coherent spin precession that is provided by the condensate. ^{17,18}

Interference dislocations

Dislocation-like phase singularities were observed in the interference patterns of IX emission. ¹⁹ The interference patterns were measured by shift-interferometry outlined earlier in Section Spontaneous coherence and Bose–Einstein condensation of indirect excitons. These singularities in the interference pattern appeared drastically different from the simulated shift-interference patterns for vortices, polarization vortices, half-vortices, skyrmions, and half-skyrmions, indicating that the observed singularity is not associated with a vortex, or polarization vortex, or half-vortex, or skyrmion, or half-skyrmion. ¹⁹

The origin of the observed singularity in the interference pattern is outlined here. Radial IX matter waves ballistically propagate from LBS sources. Each of this radial waves forms an interference pattern measured by shift-interferometry. Both analytical modeling and numerical simulation show that their combined interference patterns exhibit the phase singularities at the specific locations identified by this modeling, in agreement with the experiment ¹⁹. It is essential in this model that IXs ballistically propagate from the source; this is in accord with the experiment where the long coherence length in the IX condensate supports the long-range ballistic IX propagation.

The observed isolated interference dislocations originate from converging of the condensate-matter waves. ¹⁹ Here, the isolated dislocations indicate the dislocations separated by a significantly larger distance than the shift δx . In

contrast, dislocations separated by δx can be associated with vortices, polarization vortices, or half-vortices.

For multiple sources of IXs, our experiments show multiple interference dislocations, in agreement with our theoretical simulations. ¹⁹ All observed phase singularities disappear above the IX condensation temperature where the interference patterns become trivial with no dislocations. This is consistent with the requirement of long-range ballistic IX propagation, which is provided by the long coherence length in the condensate.

Conclusions

We overviewed studies of quantum gases of indirect excitons (IXs), also known as interlayer excitons, presenting spontaneous coherence and Bose–Einstein condensation of IXs and phenomena observed in the IX condensate. These studies were performed with IXs in GaAs heterostructures. Studies of IXs are continued both in GaAs heterostructures, which form the lowest-disorder material platform, and in van der Waals transition-metal dichalcogenide (TMD) heterostructures, which can potentially form a material platform for high-temperature quantum Bose gases of IXs³⁰.

Acknowledgments

Our studies of IXs presented in this contribution were performed in collaboration with K.L. Campman, D.S. Chemla, V.T. Dolgopolov, A.I. Filin, M.M. Fogler, N.A. Gippius, A.C. Gossard, A.T. Hammack, M. Hanson, A.A. High, Lunhui Hu, A. Imamoglu, A.L. Ivanov, A.V. Kavokin, Y.Y. Kuznetsova, J.R. Leonard, L.S. Levitov, T.C.H. Liew, P.B. Littlewood, S.V. Lobanov, A.V. Mintsev, K.S. Novoselov, T. Ostatnický, M. Remeika, A.A. Shashkin, B.D. Simons, L.E. Smallwood, M. Vladimirova, Congjun Wu, and Sen Yang, and it is a pleasure to thank my collaborators. Our studies of IXs are supported by the US Department of Energy Office of Basic Energy Sciences under Award No. DE-

FG02–07ER46449 and by National Science Foundation DMR Award No. 1905478.

References

- 1. L.V. Keldysh, A.N. Kozlov, Sov. Phys. JETP 27, 521 (1968).
- 2. E.A. Cornell, C.E. Wieman, Rev. Mod. Phys. 74, 875 (2002).
- 3. W. Ketterle, Rev. Mod. Phys. 74, 1131 (2002).
- 4. Yu.E. Lozovik, V.I. Yudson, Sov. Phys. JETP 44, 389 (1976).
- 5. L.V. Butov, A.L. Ivanov, A. Imamoglu, P.B. Littlewood, A.A. Shashkin, V.T. Dolgopolov, K.L. Campman, A.C. Gossard, *Phys. Rev. Lett.* **86**, 5608 (2001).
- 6. D. Yoshioka, A.H. MacDonald, J. Phys. Soc. Jpn. 59, 4211 (1990).
- 7. L.V. Butov, A.I. Filin, *Phys. Rev. B* **58**, 1980 (1998).
- 8. I.B. Spielman, J.P. Eisenstein, L.N. Pfeiffer, K.W. West, *Phys. Rev. Lett.* **84**, 5808 (2000).
- 9. J.P. Eisenstein, A.H. MacDonald, *Nature* **432**, 691 (2004).
- 10. Sen Yang, A.T. Hammack, M.M. Fogler, L.V. Butov, A.C. Gossard, *Phys. Rev. Lett.* **97**, 187402 (2006).
- 11. M.M. Fogler, Sen Yang, A.T. Hammack, L.V. Butov, A.C. Gossard, *Phys. Rev. B* **78**, 035411 (2008).
- 12. A.A. High, J.R. Leonard, A.T. Hammack, M.M. Fogler, L.V. Butov, A.V. Kavokin, K.L. Campman, A.C. Gossard, *Nature* **483**, 584 (2012).
- 13. A.A. High, J.R. Leonard, M. Remeika, L.V. Butov, M. Hanson, A.C. Gossard, *Nano Lett.* **12**, 2605 (2012).
- 14. S.V. Lobanov, N.A. Gippius, L.V. Butov, *Phys. Rev. B* **94**, 245401 (2016).
- 15. L.V. Butov, A.C. Gossard, D.S. Chemla, *Nature* **418**, 751 (2002).
- 16. Sen Yang, L.V. Butov, B.D. Simons, K.L. Campman, A.C. Gossard, *Phys. Rev. B* **91**, 245302 (2015).
- 17. A.A. High, A.T. Hammack, J.R. Leonard, Sen Yang, L.V. Butov, T. Ostatnický, M. Vladimirova, A.V. Kavokin, T.C.H. Liew, K.L. Campman, A.C. Gossard, *Phys. Rev. Lett.* **110**, 246403 (2013).

- 18. J.R. Leonard, A.A. High, A.T. Hammack, M.M. Fogler, L.V. Butov, K.L. Campman, A.C. Gossard, *Nature Commun.* **9**, 2158 (2018).
- 19. J.R. Leonard, Lunhui Hu, A.A. High, A.T. Hammack, Congjun Wu, L.V. Butov, K.L. Campman, A.C. Gossard, arXiv:1910.06387.
- 20. M. Alloing, M. Beian, M. Lewenstein, D. Fuster, Y. González, L. González, R. Combescot, M. Combescot, F. Dubin, *Europhys. Lett.* **107**, 10012 (2014).
- 21. L.V. Butov, L.S. Levitov, A.V. Mintsev, B.D. Simons, A.C. Gossard, D.S. Chemla, *Phys. Rev. Lett.* **92**, 117404 (2004).
- 22. R. Rapaport, G. Chen, D. Snoke, S.H. Simon, L. Pfeiffer, K. West, Y. Liu, S. Denev, *Phys. Rev. Lett.* **92**, 117405 (2004).
- 23. A.L. Ivanov, L.E. Smallwood, A.T. Hammack, Sen Yang, L.V. Butov, A.C. Gossard, *Europhys. Lett.* **79**, 920 (2006).
- 24. Sen Yang, A.V. Mintsev, A.T. Hammack, L.V. Butov, A.C. Gossard, *Phys. Rev. B* **75**, 033311 (2007).
- 25. L.S. Levitov, B.D. Simons, L.V. Butov, *Phys. Rev. Lett.* **94**, 176404 (2005).
- 26. S. Pancharatnam, *Proc. Indian Acad. Sci. A* **44**, 247 (1956).
- 27. M.V. Berry, *Proc. R. Soc. Lond. A* **392**, 45 (1984).
- 28. M.Z. Maialle, E.A. de Andrada e Silva, L.J. Sham, *Phys. Rev. B* **47**, 15776 (1993).
- 29. J.R. Leonard, Y.Y. Kuznetsova, Sen Yang, L.V. Butov, T. Ostatnický, A. Kavokin, A.C. Gossard, *Nano Lett.* **9**, 4204 (2009).
- 30. M.M. Fogler, L.V. Butov, K.S. Novoselov, High-temperature superfluidity with indirect excitons in van der Waals heterostructures, *Nature Commun.* **5**, 4555 (2014).

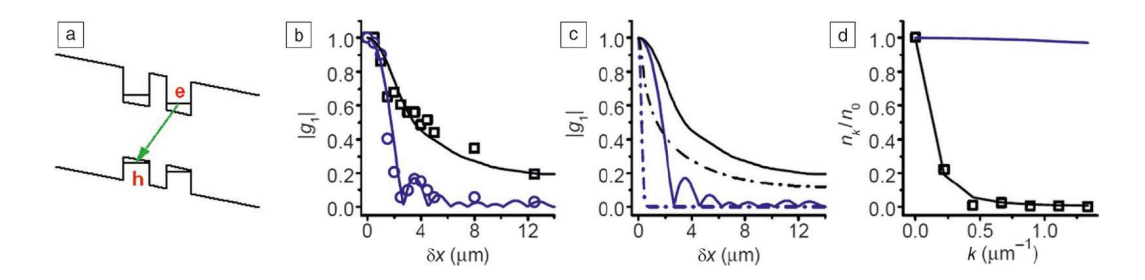


Figure 1. (a) Coupled quantum well (CQW) band diagram; e, electron; h, hole. Indirect exciton (IX) is indicated by green arrow. (b) Measured (symbols) and simulated (line plots) first-order coherence function $g_1(\delta x)$ for a quantum (black) and classical (blue) gas. $g_1(\delta x)$ quantifies coherence between excitons separated in the CQW plane by δx . (c) Simulated $g_1(\delta x)$ for a quantum (black) and classical (blue) gas with (solid) and without (dashed) convolution with the point-spread function (PSF). (d) Distribution in momentum-space n_k obtained by the Fourier transform of g_1 in (c) for a quantum (black) and a classical (blue) gas. n_0 is occupation of k=0 state. For the condensate, n_k is narrow (d) and, in turn, $g_1(\delta x)$ is broad (b,c). On the contrary, for a classical gas, n_k is broad (d) and, in turn, $g_1(\delta x)$ is narrow (b,c).

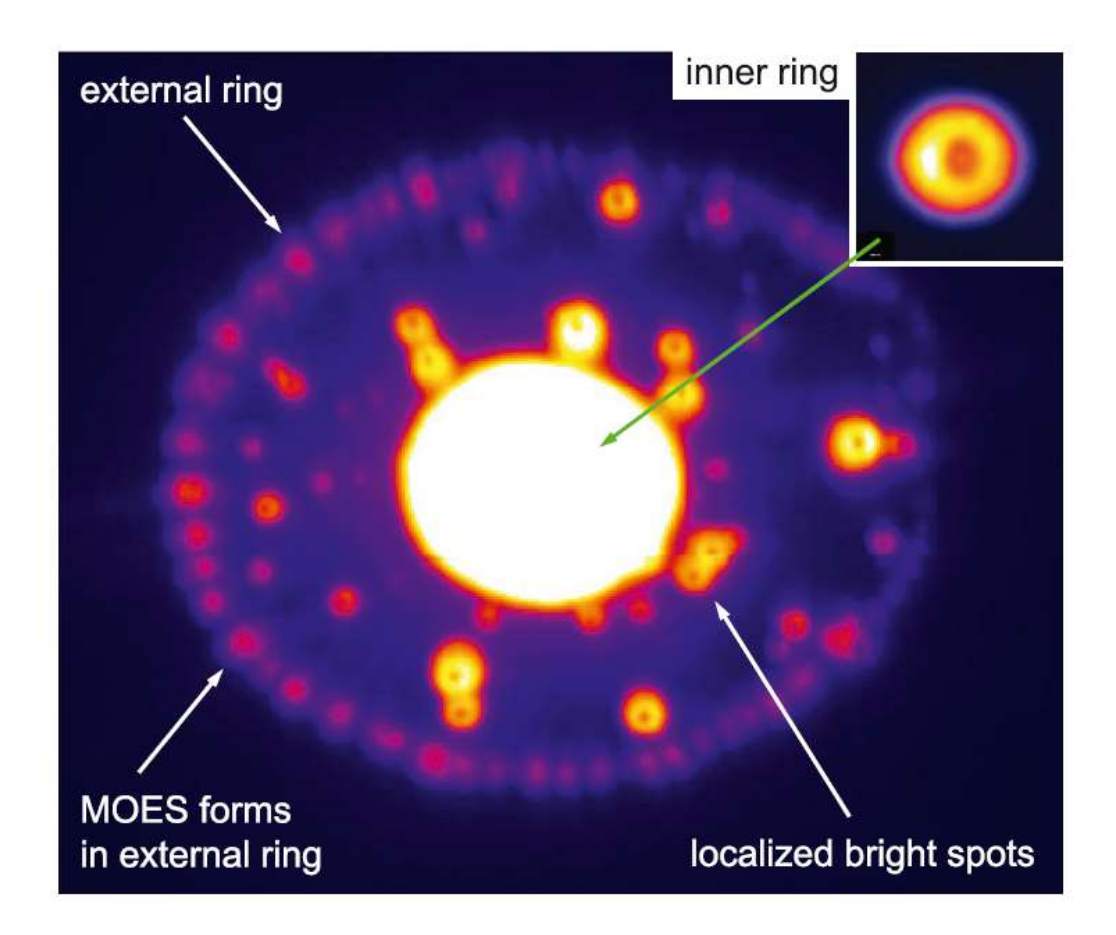


Figure 2. Indirect exciton (IX) emission pattern measured by optical imaging. The area of view is 410 μ m \times 330 μ m. The macroscopically ordered exciton state with periodic spatial modulation is observed in the external ring. ²¹

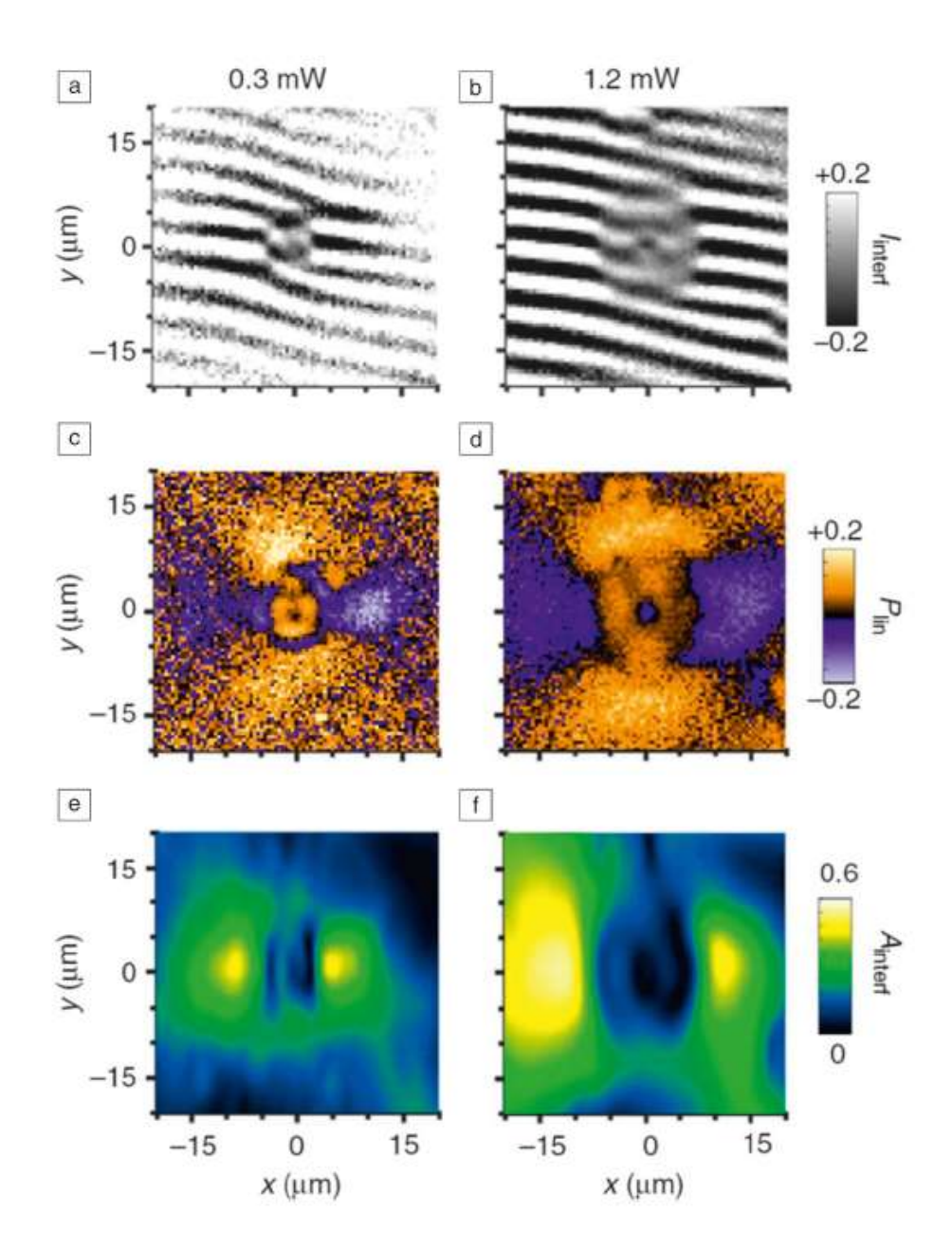


Figure 3. (a, b) Shift-interference pattern of indirect exciton (IX) emission (I_{interf}) measured by interferometry described in Section Spontaneous coherence and Bose–Einstein condensation of indirect excitons. (c, d) Linear polarization (of IX emission measured by polarization-resolved imaging. (e, f) Amplitude of interference fringes (A_{interf}) in (a–b). Excitation power 0.3 (1.2) mW for left (right). The phase shifts (a,b) correlate with the polarization pattern (c,d) and onset of IX spontaneous coherence (e,f). The correlation between the phase shift and the polarization change identifies the phase as the Pancharatnam–Berry phase acquired in a condensate of IXs. ¹⁸

Sidebar: Glossary

Commensurability effect: The commensurability effect of an exciton density wave is the suppression of fluctuations of the exciton density wave when the number of its wavelengths on a confined wave segment is an integer.

Dyakonov—Perel spin relaxation: Spin relaxation is the disappearance of nonequilibrium spin polarization. In general, spin relaxation is caused by fluctuating magnetic fields. The Dyakonov—Perel mechanism of spin relaxation is related to effective magnetic fields originating from the spin—orbit interaction in noncentrosymmetric materials. The effective magnetic field depends on the momentum and changes in time due to particle scattering. These field fluctuations cause the spin relaxation. The Dyakonov—Perel mechanism refers to the case when the scattering time is small in comparison to the inverse spin precession frequency.

Electron-hole droplets: A real-space condensate of photoexcited electrons and holes into droplets of a metallic Fermi liquid of electrons and holes, the so-called electron-hole liquid, characterized by a definite equilibrium density of electron-hole pairs.

Exciton density wave: An exciton state, dubbed the macroscopically ordered exciton state (MOES), which exhibits approximately periodic spatial modulation of the exciton density.

First-order coherence function: The correlation of two electric fields $g_1(\delta t, \delta \mathbf{r}) = \langle E(t + \delta t, \mathbf{r} + \delta \mathbf{r}) E^*(t, \mathbf{r}) \rangle / \langle E^2(t, \mathbf{r}) \rangle$ (*t* is time, **r** coordinate). In the experiments considered here, $E(t,\mathbf{r})$ is the electric field of the light emitted by excitons and the lengths of two arms of the interferometer are equal ($\delta t = 0$), therefore $g_1(\delta \mathbf{r})$ quantifies coherence between excitons separated in the coupled quantum well plane by $\delta \mathbf{r}$.

Modulational instability: The development of nearly periodic wave modulations caused by broadband perturbations.

Point-spread function (PSF): The response of an imaging system to a point source. The PSF width corresponds to the spatial resolution of the optical system.

Quantum degeneracy: (Average) occupation number of particles in a quantum state approaches and exceeds 1 for bosons or approaches 1 for fermions.